Elastic scattering of ^{6}Li at 73.7 MeV

R. Huffman,* A. Galonsky, R. Markham,† and C. Williamson‡
Cyclotron Laboratory, Michigan State University, East Lansing, Michigan 48824
(Received 6 December 1979)

Angular distributions for ^{6}Li elastic scattering at 73.7 MeV from targets of ^{58}Ni, ^{90}Zr, ^{124}Sn, and ^{208}Pb have been measured. Optical-model parameters for Woods-Saxon real and imaginary volume potentials have been found which describe the data well and exhibit both discrete and continuous ambiguities. For a fixed geometry, the dependence of the optical potentials on Z and A of the target and on the bombarding energy was investigated.

[NUCLEAR REACTIONS ^{58}Ni, ^{90}Zr, ^{124}Sn, ^{208}Pb (^{6}Li, ^{6}Li), E = 73.7 MeV; measured $\sigma(\theta)$; deduced optical-model parameters.]

I. INTRODUCTION

There have been studies of ^{6}Li elastic scattering by medium- and heavy-weight nuclei with bombarding energies between 30 and 50 MeV (Refs. 1-5) and above 100 MeV.[6] The motivation for this study was to provide optical-model parameters at an intermediate energy, namely 73.7 MeV. The parameters are presented for use in direct-reaction calculations and, when coupled with the results at higher and lower bombarding energies, may be used to investigate the systematics of ^{6}Li elastic scattering. The present study uses targets of ^{58}Ni, ^{90}Zr, ^{124}Sn, and ^{208}Pb. The dependence of the potential depths on the Z and A of the target and on the bombarding energy has been investigated.

II. EXPERIMENTAL PROCEDURE

A beam of 73.7 MeV ^{6}Li^{+++} ions was produced by the MSU sector-focused cyclotron. The beam was produced by an arc-type ion source[7] which employed the sputtering action of Ne on ^{6}Li enriched LiF pellets. The beam was transported to a 1-m scattering chamber where elastic-scattering measurements were taken. The transport system, consisting of two analyzing magnets and several quadrupole focusing magnets, produced a beam spot approximately 2 mm by 4 mm as viewed with an MgO scintillator. On-target beam currents of 1-100 nA were monitored by stopping the beam in a Faraday cup. An Ortec charge digitizer was employed to integrate the beam current from the Faraday cup in order to obtain charge measurements for each experimental point.

The targets employed in this study were isotopically enriched, self-supporting foils with average thicknesses as follows: ^{58}Ni, 3.8 mg/cm^2; ^{90}Zr, 10.2 mg/cm^2; ^{124}Sn, 5.1 mg/cm^2; ^{208}Pb, 10.3 mg/cm^2. The average thicknesses were obtained by weighing the targets with a precision balance and by measuring the surface area. An alpha-particle gauge was then used to investigate the central region of each target in order to determine thickness uniformity in the beam-spot region. The alpha-gauge measurements revealed relative variations of ±3% for the Ni, Zr, and Sn targets and ±12% for the Pb target.

Detection of the scattered ^{6}Li^{+++} ions was made by using two ΔE-E telescopes mounted symmetrically on opposite sides of the beam axis. The detectors in both telescopes were Ortec silicon surface barrier detectors with thicknesses of ~100 μm for the ΔE detector and ~1000 μm for the E detector. The angular acceptance of each telescope was defined by a collimator placed at the front of the telescope. For each telescope, the angular acceptance was 0.3° for angles less than 30° and 1° for angles greater than 30°. The detector arrangement provided two advantages over a single-telescope-plus-fixed-monitor arrangement. Continuous monitoring of any beam drift from the true beam axis was provided by comparison of the yields in the elastic peaks of the two telescopes after each measurement. For a slight misalignment, $\Delta\theta$, the average value of the two yields is correct to second order, since one angle is $\theta + \Delta\theta$ and the other is $\theta - \Delta\theta$. A difference between yields indicated that the beam had moved slightly from the original beam axis, and a realignment of the beam could be made before the next measurement. The other advantage was that the use of a second telescope produced an improvement in statistical accuracy by a factor of $\sqrt{2}$. Due to the low beam currents, the angular range of measurements was limited by a combination of time and decreasing cross section with angle.

The pulses from both telescopes were processed by the same octal ADC and were, thus, subject to the same system dead time. Two measurements for the dead time were made simultaneously using pulses from the charge digitizer and from the ADC strobe. Each set of pulses was counted by two scalers, one of which was inhibited whenever the ADC was busy. The ratio was the fractional live time. The two determinations were always within one percent of each other. A two-dimensional ΔE *vs* (E + ΔE) display was used for each telescope for particle identification and for gating of the spectrum of interest. The elastic peaks in the gated spectra had resolutions of ~400 keV (FWHM). Spectra were taken in one-degree steps from 8° to 30° and in two-degree steps for angles greater than 30°. The maximum angle measured (in the lab) was 50° for Ni, Zr, and Pb and 56° for Sn. Points taken at the start of a run were repeated at the end; agreement was always within statistics.

III. EXPERIMENTAL RESULTS

The measured ^{6}Li angular distributions are shown in Fig. 1. The indicated errors are relative errors only. Where there is no error indicated, the error is smaller then the point size. At large angles, the errors are primarily statistical due to low counting rates. At all angles there are small cross-sectional errors due to uncertainties in the settings and readouts of the angular positions of the detectors. These differ from angle to angle, since they are a function of the slope of the angular distribution. There are also small uncertainties due to possible beam drifts across the somewhat nonuniform central region of each target. The relative errors are generally $\leq \pm 4\%$ for all but the largest angles. The absolute errors

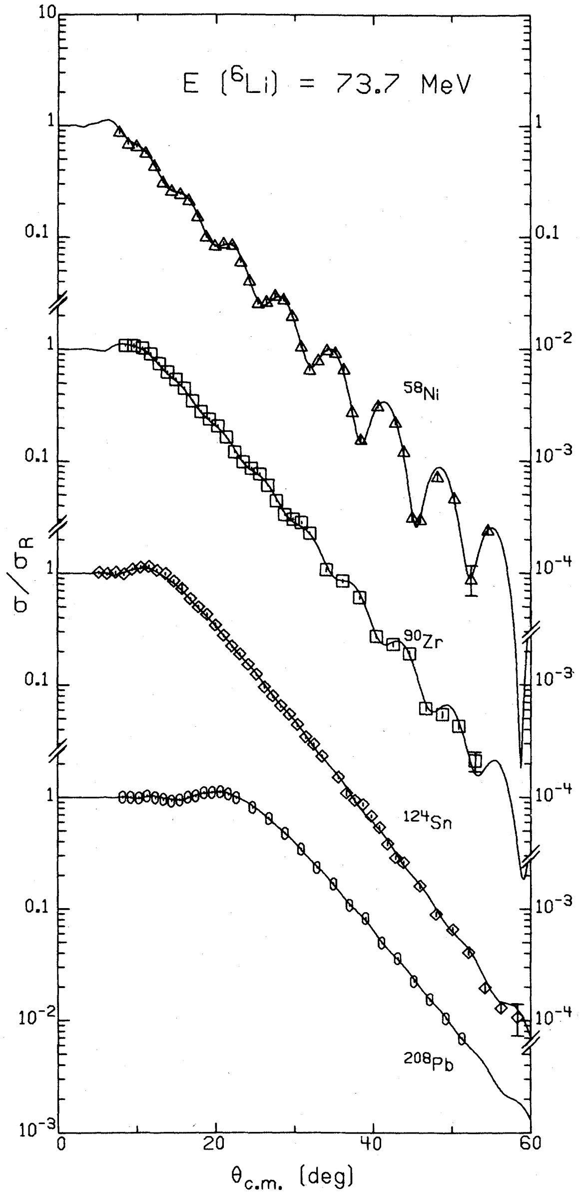

Fig. 1. Ratio-to-Rutherford angular distributions for 73.7 MeV, elastically-scattered ^{6}Li. The curves are optical-model results from the grids on V_R for each target.

are ± 5%.

At forward angles, the angular distributions are strongly dominated by the Coulomb potential. Modifications due to the nuclear potential are small and relatively insensitive to a choice of parameters. The angular distributions are thus expected to approximate Rutherford scattering at small angles. Disagreements between predicted cross sections and measured cross sections for scattering from ^{124}Sn and ^{208}Pb at small angles (~ 8% for Sn and ~18% for Pb) resulted in the need to normalize the scattering data to Rutherford scattering at the extreme forward angles ($\leq 8°$ for Sn and $\leq 12°$ for Pb). The angular distributions for ^{58}Ni and ^{90}Zr were not normalized. The measured cross sections for ^{90}Zr agreed well with predicted cross sections at the extreme forward angles. The measured cross sections for ^{58}Ni never reached a value as high as that of Rutherford scattering.

IV. OPTICAL-MODEL SEARCHES AND DISCUSSION

A. Optical-Model Search Code

The angular distributions were analyzed with the optical-model search code SGIB,[8] which is a modified version of the code GIBELUMP[9] by Perey. The nuclear potential term was a standard six-parameter, Woods-Saxon form:

$$U(r) = -V_R f_R(r) - iW_S f_I(r),$$

where

$$f_x(r) = [\,1+\exp\,(\frac{r-R_x}{a_x})]^{-1}$$

and

$$R_x = r_x A^{1/3}\,; \quad x = R,I.$$

The Coulomb potential had the form:

$$U_c(r) = 3Ze^2/r \quad \text{for } r \geq R_c,$$

$$= (3Ze^2/2R_c)(3-r^2/R_c^{\,2}) \quad \text{for } r < R_c,$$

where $R_c = r_c A^{1/3}$. In the above expressions Z and A are the target atomic number and mass number, respectively. In all searches, the Coulomb radius parameter, r_c, was kept fixed at 1.4 fm.

The search code minimized the quantity χ^2 given by

$$\chi^2 = \sum_{i=1}^{N} [\,(\sigma_{exp}(\theta_i) - \sigma_{th}(\theta_i))/\Delta\sigma_{exp}(\theta_i)]^2 \;,$$

where N is the number of experimental points.

Prior to extensive searching for optical-model solutions to the scattering data, judicious choices were made for R_m, the radius at which the asymptotic solution is matched to the internal solution of the Schrödinger equation, and for h, the step size for integration from 0 to R_m. The values chosen were determined by studying selected scattering matrix elements and large-angle differential cross sections as functions of R_m and h in the following manner. With h set at 0.1 fm, R_m was varied from 10 fm to 25 fm in steps of 1 fm. Values of the scattering matrix and cross section were approximately independent of R_m from 14 fm to 18 fm for the ^{58}Ni, ^{90}Zr, and ^{124}Sn data. Choosing R_m = 17 fm for ^{58}Ni, 16 fm for both ^{90}Zr and ^{124}Sn, and 20 fm for ^{208}Pb, h was then varied from 0.15 fm down to 0.03 fm in steps of 0.01 fm. As the step size was decreased the cross sections at even the largest angles tended to converge. The cross sections for the cases of h = 0.03 fm and h = 0.05 fm were almost identical. However, at angles where we actually had data, the cross sections were identical for values of h from 0.03 fm to 0.11 fm. To minimize computational time without risk of error a value of h = 0.1 fm was chosen for all searches.

B. ^{58}Ni

As seen in Fig. 1, the angular distribution for scattering from the ^{58}Ni target shows the greatest diffractive behavior of any of the angular distributions of the targets studied. As have been reported previously,[3,5,10–13] both discrete and continuous ambiguities exist in optical-model analyses of ^{6}Li elastic-scattering data. It was hoped that the diffractive behavior would help to eliminate some of the ambiguities which appear in analyses, and thus the ^{58}Ni data were the first data analyzed.

Searching for optical-model parameter sets which describe the ^{58}Ni data began with three independent griddings on V_R. In these griddings, V_R was varied from 10 MeV to 300 MeV in steps of 10 MeV. The first gridding was started at $V_R = 160$ MeV, and the remaining five parameters were those of Chua et al.[1] The five parameters, r_R, a_R, W_S, r_I, and a_I, were varied in pair combinations, and the final search was a simultaneous five-parameter search. The best-fit parameters from the search at $V_R = 160$ MeV were used to initiate the searches at $V_R = 150$ MeV and at $V_R = 170$ MeV, which had the same search pattern as that used for $V_R = 160$ MeV. The results from the $V_R = 150$ MeV search were used to initiate the search at $V_R = 140$ MeV, and the results from the search at $V_R = 170$ MeV were used to initiate the search at $V_R = 180$ MeV. This pattern of using the best-fit parameters of one grid point to initiate the search at the next grid point was continued to the limits of the grid. The second gridding on V_R used the parameters of Chua et al.[1] to initiate the search at each grid point. Again, the remaining five parameters were varied in pairs, and the last search was a simultaneous five-parameter search. The third gridding on V_R was a four-parameter search where r_R was kept fixed at 1.26 fm. This was done in an attempt to avoid the continuous $V_R r_R^n$ ambiguity. The remaining four free parameters were varied in pairs and then in a simultaneous four-parameter search. Finally, r_R was allowed to vary, first alone, then in a simultaneous five-parameter search.

The results of these griddings were then combined into a single grid on V_R. The parameters for a given grid point were determined by using the parameter set for the grid point which gave the lowest χ^2 of the three parameter sets for that value of V_R. Using the results from the combined grid, the real well depth was next allowed to vary, first by itself, then in a simultaneous six-parameter search. While most of the parameter sets resulting from this search were similar to those initiating the search and had approximately the same χ^2, five minima appeared where the χ^2 was reduced significantly and the parameter sets were significantly different. These five minima were investigated by gridding on V_R every 5 MeV for a distance of approximately 30 MeV on either side of each minimum. The search was a simultaneous five-parameter search on r_R, a_R, W_S, r_I and a_I, using the parameter values at the minimum as starting values. The results of this final grid are presented in Fig. 2. This grid exhibits the behavior of both the continuous ambiguity and the discrete family ambiguity. The parameter sets which correspond to the best fits for the five discrete families of potentials are listed in Table I, and the fit from Family IV is shown in Fig. 1.

The discrete family ambiguity is exhibited in Fig. 3 where three fits to the data corresponding to distinct parameter sets are presented. Each of the fits has approximately the same χ^2. The discrete ambiguity is also apparent in Fig. 2 where the parameters, which vary smoothly within a family, show discontinuities between families.

The discrete ambiguities appear to be the result of Igo ambiguities[14] and internal wave function phase-shift ambiguities.[15] The phase-shift ambiguity exists for partial waves with small ℓ values. These partial waves penetrate the nuclear surface and are reflected inside the potential well by the angular momentum barrier. As shown in Fig. 4a, moving from one solution to the next deeper solution increases the number of half waves in the potential well by one. The asymptotic phase of the wave function remains unchanged.

The Igo ambiguity is the result of partial waves with large ℓ values being scattered by nearly identical nuclear surfaces. The condition for surfaces to be nearly identical is expressed by requiring potential wells to have approximately the same values of the Igo constants[15]

$$I_R = V_R \, e^{R_R/a_R}$$

and

$$I_I = W_S \, e^{R_I/a_I} \; .$$

As seen in Fig. 4b, partial waves which see only the surfaces of the potentials contain the same number of half waves in the surface regions and have the same asymptotic phase for all potentials with constant I_R and I_I.

The values of I_R and I_I for our best-fit parameter sets are presented in Table I. I_R, with the exception of the value for the $V_R = 60$-MeV potential, varies by approximately 20%, and I_I for all solutions varies by less than 15%. The constancy of the values of I_R and I_I indicates that the surface regions must be approximately the same. For the imaginary part of the potential, it is clear from the values in Table I for W_S, r_I, and a_I that both the surface and interior regions are similar for the five solutions. We sometimes started W_S at 40 MeV, but the search always led to a value near 20 MeV. The real potential wells for three of the discrete solutions are shown in Fig. 5. Particularly for Families III and V, the potentials are almost identical beyond 6.3 fm, where the value is approximately -14 MeV.

The continuous ambiguity is exhibited in the regions near the χ^2 minima. In these regions the value of χ^2 is nearly constant over a range of V_R values. Over this range the values of the remaining five parameters vary smoothly. This smooth variation of parameters (see Fig. 2) allows for small variations of one parameter to be compensated for by small variations of other parameters.

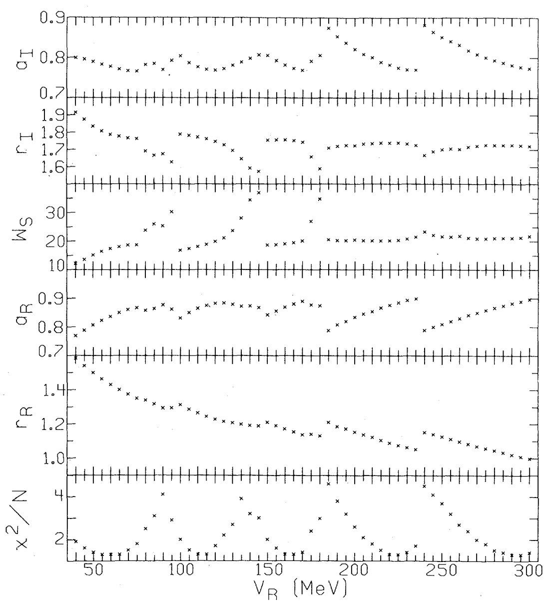

Fig. 2. Results of searches on optical-model parameters performed in fitting the ^{58}Ni scattering data. The grid on V_R shows evidence of both discrete and continuous ambiguities.

Table I. Best fit optical-model parameters from grids on V_R.

Target	Family	χ^2/N	V_R (MeV)	r_R (fm)	a_R (fm)	W_S (MeV)	r_I (fm)	a_I (fm)	σ_R (mb)	I_R (MeV)	I_I (MeV)
^{58}Ni	I	1.3	60.0	1.431	0.837	17.4	1.787	0.778	2085.	4.49×10^4	1.26×10^5
^{58}Ni	II	1.3	111.7	1.258	0.867	18.3	1.768	0.775	2065.	3.05×10^4	1.25×10^5
^{58}Ni	III	1.3	163.0	1.161	0.876	19.2	1.753	0.777	2060.	2.75×10^4	1.19×10^5
^{58}Ni	IV	1.3	223.4	1.081	0.882	20.3	1.738	0.777	2055.	2.55×10^4	1.16×10^5
^{58}Ni	V	1.3	292.0	1.015	0.885	21.2	1.726	0.779	2054.	2.47×10^4	1.12×10^5
^{90}Zr	A	3.3	63.7	1.394	0.808	84.1	1.326	0.882	2330.	1.44×10^5	7.05×10^4
^{90}Zr	B	3.3	115.2	1.337	0.744	16.3	1.705	0.897	2461.	3.62×10^5	8.12×10^4
^{90}Zr	C	3.3	152.8	1.279	0.754	17.4	1.684	0.896	2442.	3.04×10^5	7.88×10^4
^{90}Zr	D	3.4	192.5	1.235	0.757	20.2	1.642	0.909	2440.	2.86×10^5	6.58×10^4
^{90}Zr	E	3.5	240.0	1.186	0.765	22.6	1.611	0.914	2434.	2.49×10^5	6.04×10^4
^{90}Zr	F	3.5	281.9	1.166	0.761	23.7	1.597	0.919	2438.	2.70×10^5	5.69×10^4
^{124}Sn	A	2.3	163.9	1.226	0.798	21.9	1.602	0.924	2707.	3.47×10^5	1.24×10^5
^{124}Sn	B	2.3	195.0	1.093	0.880	23.6	1.577	0.928	2677.	9.51×10^4	1.12×10^5
^{124}Sn	C	2.3	223.7	1.125	0.837	20.2	1.621	0.914	2691.	1.81×10^5	1.39×10^5
^{124}Sn	D	2.3	256.8	1.127	0.813	24.6	1.562	0.938	2684.	2.56×10^5	9.89×10^4
^{124}Sn	E	2.3	290.0	1.127	0.803	24.2	1.574	0.935	2704.	3.17×10^5	1.07×10^5
^{208}Pb	A	1.3	155.0	1.359	0.667	42.4	1.335	1.030	2740.	2.69×10^7	9.16×10^4
^{208}Pb	B	1.2	183.3	1.376	0.619	17.4	1.467	1.073	2749.	9.56×10^7	5.68×10^4
^{208}Pb	C	1.2	238.0	1.340	0.629	19.5	1.450	1.068	2751.	7.24×10^7	6.10×10^4

For partial waves with small ℓ values this allows for a fixed number of half waves to remain in the potential well.[10] However, as the variations become larger, the nuclear surface is altered to a greater extent and partial waves with large ℓ values reflected from the nuclear surface see differences in the potential surfaces. This leads to differences in the scattering cross sections and a worsening of the quality of the fit. If the surface is altered too greatly, then a new family may appear whose potential surfaces have shapes nearer to the one needed to

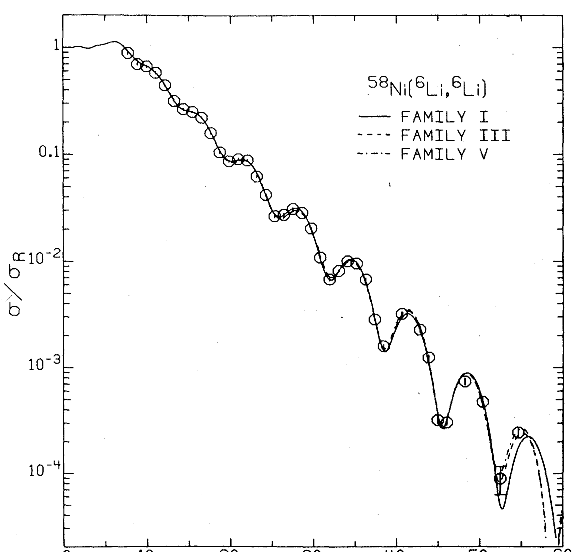

Fig. 3. Fits to the ^{58}Ni scattering data for parameter Families I, III, and V of Table I. Differences in the fits are readily discernible only beyond 52°.

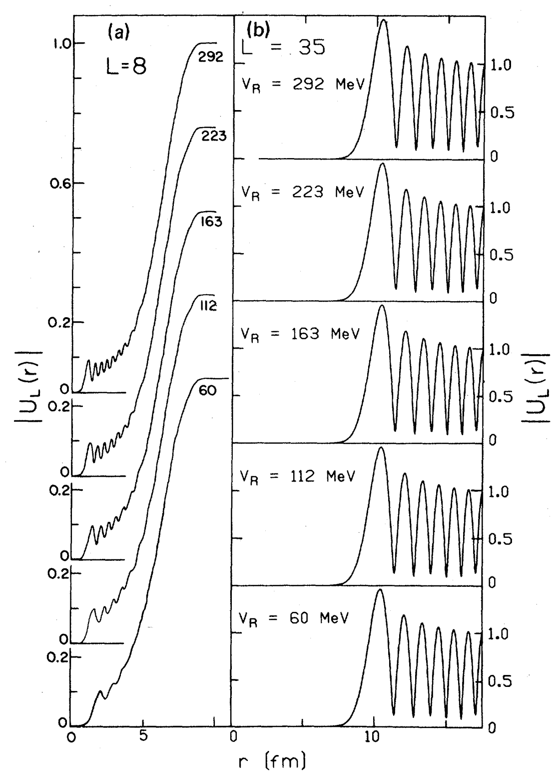

Fig. 4. (a) Radial wave functions for the five ^{58}Ni potential families (L=8) exhibit a phase shift between adjacent solutions inside the potential well. (b) Radial wave functions for the five ^{58}Ni potential families (L=35) exhibit no phase shift when scattering takes place at the nuclear surface.

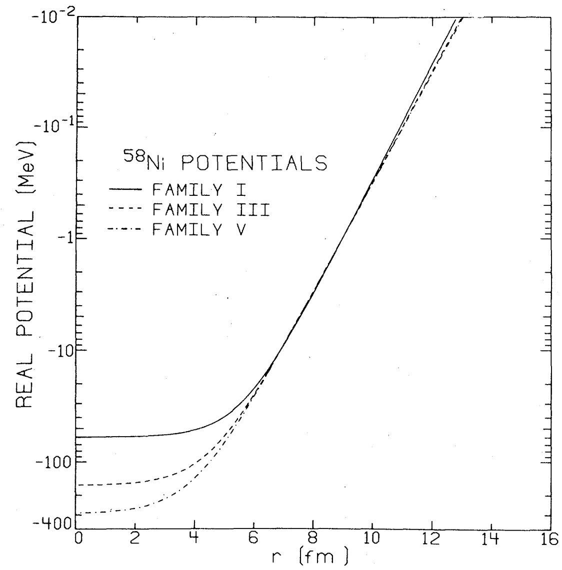

Fig. 5. The real potential wells for ^{58}Ni Families I, III, and V of Table I. The interiors of the wells are different, but the surfaces are nearly identical.

accurately reproduce the scattering.

The smooth variation of parameters within a family implies the possibility that some of the parameters may be related. It has been noted by other groups that V_R and r_R appear to be related by $V_R r_R^n \sim$ constant, where the constant is different for different families. Reported values for n are $n \sim 1$-2.[1,10,11,13] In our study n varies from 1.6 to 4.0. For Families I through V the values of n are 4.0, 2.7, 2.0, 1.8 and 1.6, respectively.

C. ^{90}Zr, ^{124}Sn, and ^{208}Pb

The results of the analysis for ^{58}Ni provided the bases for the analyses of the data sets of the other targets. Each of the five solutions for ^{58}Ni was used as a starting point for a search on the data of each of the other three targets. Final grids on V_R were performed (ΔV_R = 5 MeV) as in the case of ^{58}Ni. The grids on V_R extended from V_R = 40 MeV to 300 MeV for ^{90}Zr and from V_R = 150 MeV to 300 MeV for ^{124}Sn and ^{208}Pb. The solutions produced by the gridding are presented in Table I. As in the ^{58}Ni case, both discrete and continuous ambiguities were observed.

Searches with the ^{90}Zr data produced six discrete families. The fit from Family E is shown in Fig. 1. Over a range of V_R values each family produced a continuous ambiguity, where the remaining parameters varied smoothly and produced only small changes in χ^2. The correlation of V_R with r_R as $V_R r_R^n \sim$ constant was evident with $n \sim 1.6$-2 for all families except Family A, where n = 7. The Igo constant I varies by approximately 30% amongst the solutions, excluding Family A, and I_I varies by less than 50%.

The grid on V_R from 150 MeV to 300 MeV produced five solutions for the ^{124}Sn data. The fit produced by Family C is shown in Fig. 1. The values of I_I vary by approximately 40%. The large variations in I_R, a factor of 3.5, indicate that the surface regions for the real potentials have more variation for ^{124}Sn, as can be seen in Fig. 6, than for ^{58}Ni, Fig. 5. For Families A through E, the values of n for the continuous ambiguity are 15, 1.3, 2.8, 1.2, and 4.2, respectively.

The grid on V_R from 150 MeV to 300 MeV produced three solutions for the ^{208}Pb data. The Family-C fit is shown in Fig. 1, and the best-fit parameters are listed in Table I. As in the case of ^{124}Sn, the values of I_R for the ^{208}Pb solutions vary by a factor of ~ 3.6. The values of I_I for ^{208}Pb vary by a factor of ~ 1.8. The values of n for Families A, B, and C are 4.6, 1.9, and 2.1, respectively. The non-uniqueness of the surface regions for the ^{124}Sn and the ^{208}Pb solutions may be the result of the influence of the Coulomb interaction on the scattering. The larger Z of the ^{124}Sn and ^{208}Pb nuclei and the limited angular range of data for all the nuclei studied produces a stronger Coulombic influence on the ^{124}Sn and ^{208}Pb data than on the ^{58}Ni and ^{90}Zr data. The stronger Coulombic influence reduces the sensitivity of the predicted cross sections to changes in the nuclear potential parameters.

D. Fixed-Geometry Searches

In order to investigate the mass and charge dependences of the potential wells, searches were performed on the Zr, Sn, and Pb data in which only the potential depths, V_R and W_S, were varied. The geometry parameters were chosen from the Ni families and fixed for the searches in two ways.

The first set of searches used the light-ion convention to define the radius of the potential well, $R_x = r_x A^{1/3}$, where r_x is either the real or the imaginary radius parameter. The quantities which were fixed for these searches were the two radius parameters, r_R and r_I, and the two diffusivities, a_R and a_I. The parameter values were those of the five families found for ^{58}Ni and listed in Table I. Separate searches were performed for each family. The results of the searches are presented in Fig. 7. It was assumed that the potentials had an A and Z dependence of the form $V_R = C_1 + C_2 Z/A^{1/3}$ and $W_S = C_3 + C_4 Z/A^{1/3}$.[5,16] No investigation of a nuclear potential symmetry term of the form (N-Z)/A was performed. Since ^{6}Li has an isospin of zero such a term is

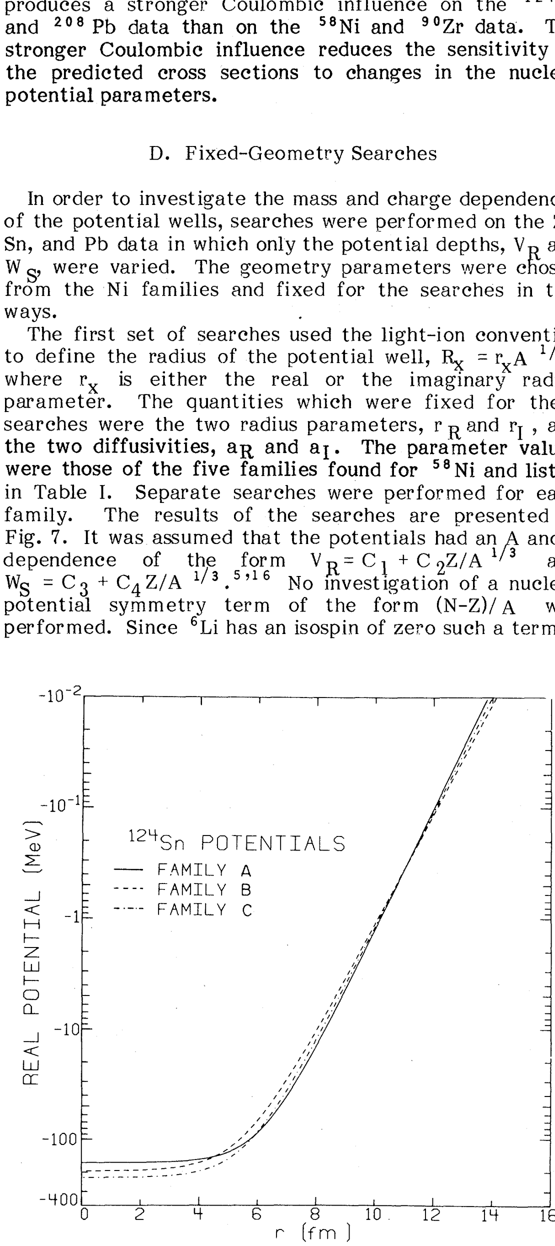

Fig. 6. The real potential wells for ^{124}Sn Families A, B, and C of Table I. The interiors and the surfaces of the wells are different.

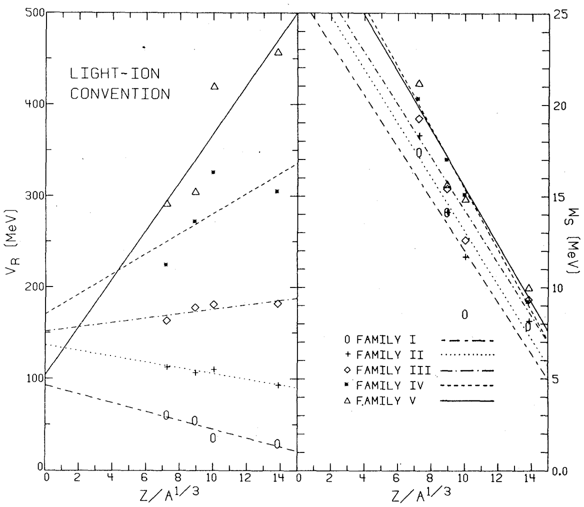

Fig. 7. Real and imaginary well depths, V_R and W_S, from light-ion convention, constant-geometry searches as a function of $Z/A^{1/3}$. The solid lines are the "best fit" results of the parameterization discussed in the text.

not expected. The "best fits" for this parameterization are shown in Fig. 7 for each family, and the values for V_R, W_S, C_1, C_2, C_3, and C_4 are given in Table II. As seen in Fig. 7, this linear parameterization of the real well depth is reasonably appropriate. For Families I and II, the potentials decrease as $Z/A^{1/3}$ increases. This result is different from the result for proton scattering, where V_R increases as $Z/A^{1/3}$ increases.[17] The linear parameterization of the imaginary well depth appears to describe the data particularly well for Family IV and reasonably well for Family V. For the other three families, the points for Ni, Zr, and Sn are fairly linear with steeper slopes than shown, but the Pb points are then relatively high. Of course, 19 of the 20 points fall within a narrow band, and a single line would come within 2 MeV of each of them. All families have a monotonic decrease in W_S with increasing $Z/A^{1/3}$.

The second set of searches used the heavy-ion convention to define the potential well radii, $R_X = r'_X(A^{1/3} + 6^{1/3})$, where the value of r'_X is fixed. Since the two radii for ^{58}Ni have given values for each family regardless of which convention is used, r'_X was determined from the relation $r'_X(58^{1/3} + 6^{1/3}) = r_X\, 58^{1/3}$. Again the diffusivities used were those from the ^{58}Ni analysis, and searches were performed for the geometries of all five ^{58}Ni families. The results of the searches are presented in Fig. 8. The parameterization of the potentials for this set of searches has the form $V_R = C'_1 + C'_2 Z/(A^{1/3} + 6^{1/3})$

Table II. "Best fit" fixed geometry search results and coefficients for the parameterization of the Z and A dependence of the potentials. The parameterization is defined in the text.

Light-Ion Convention									
Family	Potential	^{58}Ni	^{90}Zr	^{124}Sn	^{208}Pb	C_1 (MeV)	C_2 (MeV)	C_3 (MeV)	C_4 (MeV)
I	V_R (MeV)	60.0	54.0	35.2	29.1	92.4	-4.8		
	W_S (MeV)	17.4	14.1	8.5	7.9			26.1	-1.4
II	V_R (MeV)	111.7	105.5	108.9	92.0	136.3	-3.1		
	W_S (MeV)	18.3	14.1	11.6	8.1			27.8	-1.5
III	V_R (MeV)	163.0	177.6	180.8	182.0	151.4	2.4		
	W_S (MeV)	19.2	15.4	12.6	9.3			28.6	-1.4
IV	V_R (MeV)	223.4	271.1	324.8	304.2	170.3	11.1		
	W_S (MeV)	20.3	17.0	15.1	9.2			32.0	-1.7
V	V_R (MeV)	292.0	305.0	419.8	457.6	103.8	26.5		
	W_S (MeV)	21.2	15.7	14.9	10.0			31.2	-1.6

Heavy-Ion Convention									
Family	Potential	^{58}Ni	^{90}Zr	^{124}Sn	^{208}Pb	C'_1 (MeV)	C'_2 (MeV)	C'_3 (MeV)	C'_4 (MeV)
I	V_R (MeV)	60.0	84.9	93.5	138.6	- 5.0	13.6		
	W_S (MeV)	17.4	20.0	17.5	19.4			16.8	0.24
II	V_R (MeV)	111.7	170.1	203.6	340.2	- 87.5	40.2		
	W_S (MeV)	18.3	21.7	18.9	21.8			16.7	0.48
III	V_R (MeV)	163.0	253.0	313.7	579.9	-215.2	74.3		
	W_S (MeV)	19.2	22.7	19.5	24.1			16.1	0.72
IV	V_R (MeV)	223.4	349.3	438.4	897.4	-407.5	121.1		
	W_S (MeV)	20.3	23.8	19.6	25.8			16.1	0.86
V	V_R (MeV)	292.0	480.7	660.6	1298.1	-638.1	180.9		
	W_S (MeV)	21.2	25.7	22.9	27.5			17.7	0.92

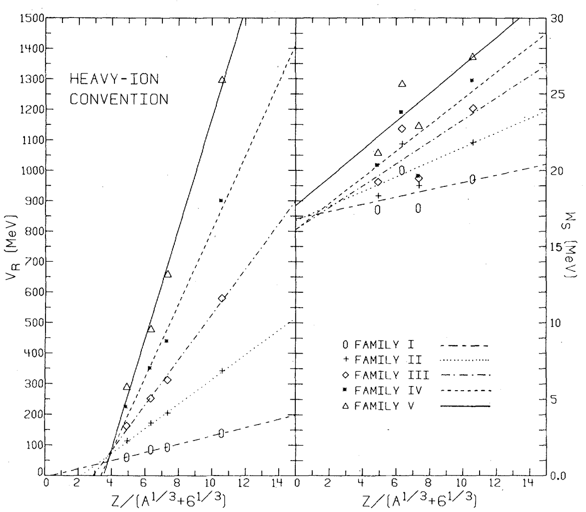

Fig. 8. Real and imaginary well depths, V_R and W_S, from heavy-ion convention, constant-geometry searches as a function of $Z/(A^{1/3}+6^{1/3})$. The solid lines are the "best fit" results of the parameterization discussed in the text.

and $W_S = C_3' + C_4' Z/(A^{1/3} + 6^{1/3})$. The "best fits" for this parameterization are presented in Fig. 8 for each family, and the values of V_R, W_S, C_1', C_2', C_3', and C_4' are given in Table II. For the real well depth this parameterization gives an accurate description of the results of the searches; for all five families the fits are very good. The intersection of the lines raises the question of whether the discrete ambiguity all but disappears for targets having an abcissa $\cong 4.0$, say ^{40}Ca or ^{45}Sc, where a real well depth of about 70 MeV is indicated for four of the families. We offer no answer to this question. The fits for the imaginary well depth represent the data fairly well.

Figures 7 and 8 should permit interpolation and extrapolation to obtain optical-model parameters for targets other than the four studied here. Although either of the two methods of defining radii produced fits useable for this purpose, a comparison of Figs. 7 and 8 shows that straight lines fit the points for the real well better when the heavy-ion radius convention is used. For the imaginary well we cannot make a choice between the two. Another point favoring the heavy-ion choice is that the searches on the Zr, Sn, and Pb data more often produced a lower χ^2 with the heavy-ion than with the light-ion convention.

E. Energy Dependence

The energy dependence of the optical potential parameters was investigated by analyzing the ^{58}Ni, ^{124}Sn, and ^{208}Pb data of Chua et al.[1] at E_{Lab} = 50.6 MeV. Since the energy dependence of the potentials is meaningful only if common geometries are used, the data of Chua et al. were analyzed by using some of the geometries found here, that is at 73.7 MeV, and searching on the well depths only. For each target the geometries of three of the families of Table I were examined using both the light-ion convention and the heavy-ion convention. Contrary to the optical model for protons, these calculations show an increase in V_R with an increase in bombarding energy in all cases except the ^{208}Pb, Family C, light-ion case. In all cases $|dV_R/dE| \le 5$. The energy dependences for the imaginary potentials are less conclusive except that the variations are small, $|dW_S/dE| \le 0.5$.

The results of a fixed-geometry grid on V_R (ΔV_R =5 MeV) with W_S being varied are shown in Fig. 9. In this illustration the χ^2 minimum occurs for $V_R \sim 150$ MeV and $W_S \sim 19$ MeV, whereas the Family-III solution at the higher bombarding energy, 73.7 MeV, has V_R = 163 MeV, W_S = 19.2 MeV. The figure clearly shows that there is no χ^2 minimum in sight for $V_R > 163$ MeV; V_R does not decrease with increasing ^{6}Li energy.

V. CONCLUSIONS

The elastic scattering of ^{6}Li at E = 73.7 MeV can be well described by using the optical model. The present analysis contains both discrete and continuous ambiguities which could not be resolved. Even if data were obtainable at larger angles the ambiguities would likely remain because the rainbow angles[18] are too large. For none of our potentials, even the shallowest potential with the lightest target, Family I of Table I, does the angular distribution cease oscillating with angle and exhibit a structureless, approximately exponential falloff characteristic of a nuclear rainbow.[18] With ^{6}Li at a higher energy, 135 MeV, scattered from a lighter target, ^{28}Si, there was rainbow scattering and a partial resolution of ambiguities was possible.[19]

The results of fixed-geometry searches show, for the light-ion radius convention, that potential depths depend

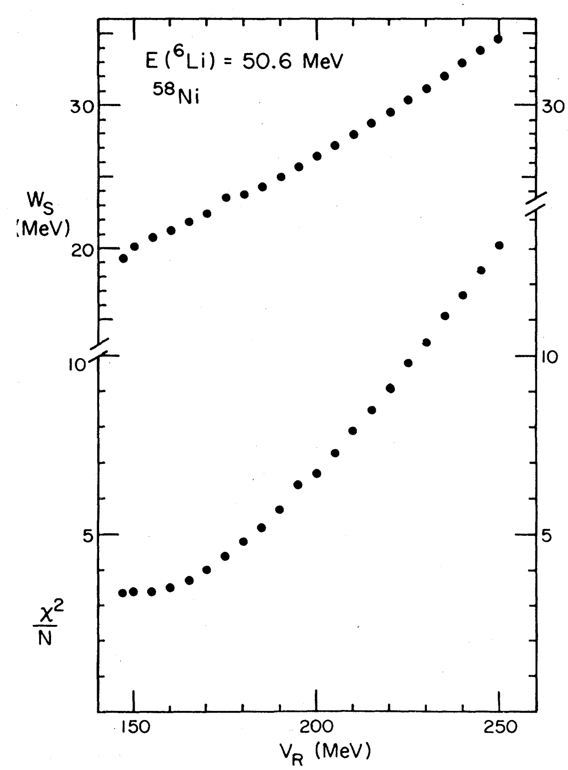

Fig. 9. Grid on V_R using the ^{58}Ni light-ion convention, Family-III (Table I) geometry. The data used are from Chua et al.[1] The 73.7-MeV value for V_R was 163 MeV. As V_R is increased above 163 MeV the quality of the fit worsens; i.e. χ^2 increases.

linearly on $Z/A^{1/3}$ for all five families with W_S always decreasing sharply with this Coulomb parameter. For the heavy-ion radius convention the potential depths are well fitted by a linear dependence on $Z/(A^{1/3}+6^{1/3})$ with W_S increasing slowly.

The energy dependence of the real potential depth for ^{58}Ni is that of an increase with increasing bombarding energy. The results for the imaginary well depth depend upon the geometry used, but the magnitude of any variation with energy is much less than for the real depth.

Grateful acknowledgment is herewith given to the National Science Foundation for its support under Grant No. Phy-7822696. We would like to thank Dr. D.A. Goldberg for calculating the relevant nuclear rainbow angles and discussing the results with us.

---

*Present address: Department of Physics and Astronomy, University of Massachusetts, Amherst, Mass. 01002.

†Present address: Xerox Corporation, Webster, N.Y. 14580.

‡Present address: IBM Corporation, Rochester, Minn. 55901.

[1] L.T. Chua, F.D. Becchetti, J. Janecke and F.L. Milder, Nucl. Phys. A273, 243 (1976).

[2] V.I. Chuev, V.V. Davidov, B.G. Novatskii, A.A. Ogloblin, S.B. Sakuta, and D.N. Stepanov, J. Phys. (Paris) 32 Suppl. 11-12, C6-157 (1971).

[3] R.J. Puigh and K.W. Kemper, Nucl. Phys. A313, 363 (1979).

[4] K.W. Kemper, A.F. Zeller, T.R. Ophel, D.R. Hebbard, A. Johnston, and D.C. Weisser, Nucl. Phys. A320, 413 (1979).

[5] R.I. Cutler, M.J. Nadworny, and K.W. Kemper, Phys. Rev. C 15, 1318 (1977).

[6] P. Schwandt, P.P. Singh, A. Nadasen, G. Adams, F.D. Becchetti, J. Janecke, and W. Ploughe, Bull. Am. Phys. Soc. 22, 633 (1977).

[7] E.D. Hudson and M.L. Mallory, IEEE Trans. Nucl. Sci., NS-23 1065 (1976).

[8] R.R. Doering, A.I. Galonsky, and R.A. Hinrichs, J. Comput. Phys. 12, 498 (1973).

[9] F.G. Perey, Optical-model search code, ORNL, and modified by R.M. Haybron, Cleveland State University, 1966.

[10] W. Schmidt and U. Strohbusch, Nucl. Phys. A159, 104 (1970).

[11] G. Bassani, N. Saunier, B.M. Traore, and J. Raynal, Nucl. Phys. A189, 353 (1972).

[12] J.E. Poling, E. Norbeck, and R.R. Carlson, Phys. Rev. C 5, 1819 (1972).

[13] J.E. Poling, E. Norbeck, and R.R. Carlson, Phys. Rev.C 13, 648 (1976).

[14] G. Igo, Phys. Rev. Lett. 1, 72 (1958).

[15] R.M. Drisko, G.R. Satchler, and R.H. Bassel, Phys. Lett. 5, 347 (1963).

[16] C.B. Fulmer, J.B. Ball, A. Scott, and M.L. Whiten, Phys. Rev. 181, 1565 (1969).

[17] F.D. Becchetti and G.W. Greenlees, Phys. Rev. 182, 1190 (1969).

[18] D.A. Goldberg and S.M. Smith, Phys. Rev. Lett. 29, 500 (1972). In general, the rainbow angles are too large and the effect too weak. (D.A. Goldberg, private communication.)

[19] R.M. DeVries, D.A. Goldberg, J.W. Watson, M.S. Zisman, and J.G. Cramer, Phys. Rev. Lett. 39, 450 (1977).